



Full length article

Creep properties and deformation mechanisms of a Ni₂Co₁Fe₁V_{0.5}Mo_{0.2} medium-entropy alloy

Wei Jiang^a, Yang Cao^{a,*}, Shengyun Yuan^b, Yong Zhang^b, Yonghao Zhao^{a,*}^a Nano and Heterogeneous Materials Center, School of Materials Science and Engineering, Nanjing University of Science and Technology, Nanjing 210094, China^b Herbert Gleiter Institute of Nanoscience, Nanjing University of Science and Technology, Nanjing 210094, China

ARTICLE INFO

Keywords:

Medium-entropy alloy
High temperature creep
Deformation mechanism
Dislocation configuration
Grain refinement

ABSTRACT

The creep properties of a Ni₂Co₁Fe₁V_{0.5}Mo_{0.2} medium-entropy alloy (MEA) in the temperature range 973–1073 K, and under the stresses 150–200 MPa, have been investigated in detail. The Ni₂Co₁Fe₁V_{0.5}Mo_{0.2} MEA possesses excellent creep properties at 973 K/150 MPa and 973 K/175 MPa. The stress exponent n was calculated to be 3.1 at 973 K, suggesting the dominance of viscous dislocation glide mechanism in creep deformation. The activation energy for creep deformation was measured to be 456.3 kJ·mol⁻¹, which is comparable to the activation energy for self-diffusion of Mo, indicating a strong effect of Mo diffusion on viscous dislocation glide. Detailed transmission electron microscopy analysis reveals: (1) increased stress and strain can alter the dislocation configurations and promote dislocation climb, and thus to increase the creep rate; (2) increased temperature and strain can lead to active recovery and recrystallisation, and thus to cause grain refinement.

1. Introduction

Since the first emergence of high-entropy alloys (HEAs) and medium-entropy alloys (MEAs) in 2004, a new horizon for designing materials with exceptional properties is opened [1–6]. Extensive experimental and theoretical work have been conducted to reveal the excellent mechanical properties and interesting deformation mechanisms of many HEAs/MEAs at ambient and cryogenic temperatures [7–9]. For example, Moon et al. [10] reported a Co_{17.5}Cr_{12.5}Fe₅Ni₁₀Mo₅ MEA exhibiting excellent combination of strength and ductility in the wide temperature range of 0.5–298 K, and discovered phase-transformation anomaly and discontinuous plastic flow at cryogenic temperatures. To date, it is known that under the combined effects of sluggish lattice diffusion [11], severe lattice distortion [3,12], short-range ordering [13], incipient concentration waves [14], HEAs/MEAs are capable of sustaining very high densities of dislocations and/or nanotwins, and thus stimulating excellent combinations of strength and ductility [14–17]. Based on this concept, Chang et al. [18] added small mass fractions of Si to the CrCoNi base-alloy to further increase the lattice distortion, as a result both strength and ductility were increased simultaneously.

Considering the broad industrial applications of metallic materials, engineers and researchers for sure have also looked into various engineering properties of HEAs/MEAs. For example, Shukla and Mishra [19]

processed an ultrafine grained CoCr_{1.3}Ni MEA with excellent high cyclic fatigue properties; Yang et al. [20] reported a CrCoNi MEA with outstanding fracture toughness comparing to many known MEAs and HEAs [21]. Recently, scientific explorations on the high temperature properties of HEAs/MEAs have also gained strong momentum [22–25]. As an important part of the high temperature properties of metallic materials, creep properties cannot be overlooked. Xie et al. [26] attributed the strong creep resistance and long creep lifetime of a CoCrNi MEA at 973 K to the lowered stacking fault energy (SFE) in conjunction with strong local lattice distortions, and the resultant strong interactions between stacking faults (SFs) and solute atoms. Kang et al. [27] reported the transition of rate-controlling mechanism from dislocation climb to viscous glide with increasing stress, and revealed the influence of large atomic size misfit on viscous glide of dislocations. Rozman et al. [28] found that the CoCrFeNi MEA shows unusual double minimum creep rate behavior (usually found in single crystal Ni-base superalloys) at 600–650 °C under the stresses of 120–189 MPa. Rozman et al. [28] suggest that the nucleation and growth of Cr-rich M₂₃C₆ carbides and σ precipitates are the cause for the undulation of creep rate with respect to the increasing strain. Cao et al. [29] revealed the abnormally high stress exponent ($n = 8.9$ –14) and increased creep activation energy ($Q = 380$ kJ·mol⁻¹) for a CoCrFeMnNi HEA crept under high stresses, and attributed the phenomenon to the coordinative contribution of dynamic

* Corresponding authors.

E-mail addresses: y.cao@njust.edu.cn (Y. Cao), yhzhao@njust.edu.cn (Y. Zhao).<https://doi.org/10.1016/j.actamat.2022.118590>

Received 1 June 2022; Received in revised form 8 November 2022; Accepted 4 December 2022

Available online 8 December 2022

1359-6454/© 2022 Acta Materialia Inc. Published by Elsevier Ltd. All rights reserved.

recrystallization and again dynamic precipitation of Cr-rich $M_{23}C_6$ carbides and σ phases. Cao et al. [30] also explored the effect of Al addition on creep properties of $Al_xCrMnFeCoNi$ HEAs, and found that adding an appropriate amount of Al can enhance the creep resistance, e.g. $Al_{0.4}CrMnFeCoNi$ HEA, due to solution strengthening and secondary phase strengthening effects; but an excess amount of Al will deteriorate the creep properties, e.g. $Al_{0.6}CrMnFeCoNi$ HEA, due to increased SFE and lowered activation energy. As an extreme example, Tsao et al. [31] added a large number of elements to make the novel high entropy superalloy, $Ni_{47.9}Al_{10.2}Co_{16.9}Cr_{7.4}Fe_{8.9}Ti_{5.8}Mo_{0.9}Nb_{1.2}W_{0.4}C_{0.4}$, which exhibits excellent creep properties comparable to that of the conventional superalloy CMSX-2 ($Ni_{67.4}Al_{12.5}Co_5Cr_9Ti_{1.2}Mo_{0.4}Ta_2W_{2.5}$).

In reviewing the aforementioned HEAs, MEAs and many conventional high temperature alloys [32–42], it is apparent that solid solution strengthening and precipitation strengthening are popular methods for improving high temperature properties, including creep properties. However, precipitation strengthening is usually associated with lowered entropy and sometimes drastic drop in ductility. Therefore, it is preferred to adopt the solid solution strengthening method, so that the ductility and the high entropy nature of the materials are sustained. According to literatures [13,25,43,44], Mo, V, W and Nb are commonly used solutes in high temperature solid solutions, because of their high melting points. Thus, our previous work adopted the solid solution strengthening concept by adding V and Mo to the non-equiatomic $Ni_2Co_1Fe_1V_{0.5}Mo_{0.2}$ MEA, and investigated its high temperature properties and deformation mechanisms [44]. The work shows that the strong solute pinning effect on forest dislocations stimulates the strain hardening effect even at high temperatures up to 800 °C [44]. Provided that the creep strength relies on the balance between strain hardening and recovery, it makes us wonder if the high strain hardening capability of the $Ni_2Co_1Fe_1V_{0.5}Mo_{0.2}$ MEA could grant desirable creep properties.

In present work, we continue the study on the high temperature properties of the non-equiatomic $Ni_2Co_1Fe_1V_{0.5}Mo_{0.2}$ MEA with the face-centered cubic (fcc) structure, but the research focus is shifted to the high temperature creep properties. In examining available deformation maps of many alloys [45–48], it is found that a high homologous temperature above 0.5 and a normalized shear stress (by shear modulus) at $\sim 10^{-3}$ together can stimulate power-law creep for metallic materials. Therefore, creep behaviors of the $Ni_2Co_1Fe_1V_{0.5}Mo_{0.2}$ MEA are investigated at the temperature range 973–1073 K and in the stress range 150–200 MPa corresponding to the homologous temperatures 0.58 – 0.64 and normalized stresses 1.56×10^{-3} – 1.17×10^{-3} , respectively. The stress exponent and activation energy for creep are calculated based on tensile creep tests. Detailed transmission electron microscopy (TEM) analysis is conducted to characterize the microstructural evolutions for probing the immanent deformation mechanisms.

2. Experiments

The $Ni_2Co_1Fe_1V_{0.5}Mo_{0.2}$ alloy ingot was prepared by melting 99.5% purity raw materials in a medium frequency vacuum induction furnace, and was re-melted twice to ensure the homogeneous elemental distribution. The ingot was hot-forged at 1273 K to eliminate casting flaws, and subsequently annealed at 1323 K for 8 h. Dog-bone shaped tensile creep specimens with a gage length of 25 mm and a diameter of 5 mm were machined from the as-annealed ingot. CTM504-B1 electronic high temperature creep and rupture testing machine was employed for tensile creep tests in the temperature range of 973–1073 K under initial applied stresses of 150–200 MPa. A variable displacement transducer extensometer was attached to the two bulges on the dog-bone shaped specimen for tensile strain measurement. The tensile creep tests were conducted in an electrical resistance heating furnace. The temperature surrounding the specimen was increased at a step of ~ 5 °C/min until the specified test temperature. The specimen was then held at the test temperature for ~ 30 min prior to tensile loading. Once the temperature

of the specimen stabilized, the tensile load was applied at the rate of 25 N/s until the specified load, and the load was held still for creep deformation. The test temperature was monitored with an accuracy of ± 1 K, by three independent contacting thermocouples which are respectively placed at the middle and two ends of the specimen gage.

Electron back-scattered diffraction (EBSD), scanning electron microscopy (SEM), energy-dispersive spectrometer (EDS) and TEM techniques were utilized to analyze the microstructures and composition of the $Ni_2Co_1Fe_1V_{0.5}Mo_{0.2}$ MEA. Both EBSD and EDS specimens were electropolished to mirror-like surface finish in an electrolyte containing 90% acetic acid and 10% perchloric acid, with an applied voltage of 35 V and polishing time of 45 s, in a Buehler ElectroMet-4 polisher. TEM observations were conducted in an FEI-Tecna G² 20 S-TWIN microscope operating at 200 kV. The TEM specimens were prepared by grinding the deformed gage part down to 50 μ m thickness and then punched into discs with a diameter of 3 mm. The discs were electro-polished in an aqueous electrolyte containing 10% perchloric acid, 20% glycerol and 70% methanol, at -20 °C, by a twin jet electro-polishing system with an applied voltage of 15 V.

3. Results

3.1. Initial microstructures

The EBSD map in Fig. 1a shows the microstructure of the as-annealed $Ni_2Co_1Fe_1V_{0.5}Mo_{0.2}$ MEA which composes of coarse grains mostly in millimeter sizes. The SEM-EDS maps, as shown in Fig. 1b, indicate that the elemental distributions of Ni, Co, Fe, V and Mo in the MEA are uniform without apparent elemental segregation or secondary phase particles.

3.2. Creep properties

Fig. 2a presents the creep strain vs. time curves for the $Ni_2Co_1Fe_1V_{0.5}Mo_{0.2}$ MEA tested at the temperatures of 973, 1023 and 1073 K, and under constant applied stresses of 150, 175 and 200 MPa. The schematic drawing of tensile creep specimen is illustrated in the inset in Fig. 2a. Provided that many MEAs and HEAs have ruptured in 150 h as shown in Fig. 2b, each creep test in this work was lasted to sample fracture or 168 h whichever came first, for clear illustration and close comparison of data. According to Fig. 2a, the samples tested at 1073 K/150 MPa, 1023 K/150 MPa and 973 K/200 MPa fractured at 5.55, 54 and 128 h, respectively. Fracture did not occur for the 973 K/175 MPa and 973 K/150 MPa samples in the test period of 168 h. The reader is referred to Table S1 in the Supplementary material for a list of creep properties of the $Ni_2Co_1Fe_1V_{0.5}Mo_{0.2}$ MEA. Apparently, an increase in either creep temperature or applied stress leads to earlier plastic instability and rupture. In high temperature creep, grain boundary separation, microcracks, cavities, and voids are the common microscopic plastic instabilities in concern; Necking and cracks are the commonly observed macroscopic plastic instabilities prior to rupture [49–52]. Provided that the strain rates are low and the deformation temperatures are very high above 973 K in the current creep tests, strain rate sensitive plastic instabilities such as the adiabatic shear band are omitted [53–55].

Fig. 2b compares creep strain vs. time data of the present MEA with other HEAs and MEAs. As shown in Fig. 2b, at the creep temperature 923 K the CrMnFeCoNi HEA ruptured in 3.9 h [27], and at the creep temperature 1073 K the CoCrNi MEA ruptured in 12.4 h [26]. An appropriate addition of Al effectively enhanced the creep properties of the $Al_{0.4}CrMnFeCoNi$ HEA, but an excess amount of Al content, e.g. $Al_{0.6}CrMnFeCoNi$, prejudiced the creep resistance [30]. Encouragingly, the present single phase $Ni_2Co_1Fe_1V_{0.5}Mo_{0.2}$ MEA exhibits superior creep resistance in comparison to other alloys despite the harsh test conditions of high temperature and stress.

The creep curves shown in Fig. 2a are different from the traditional

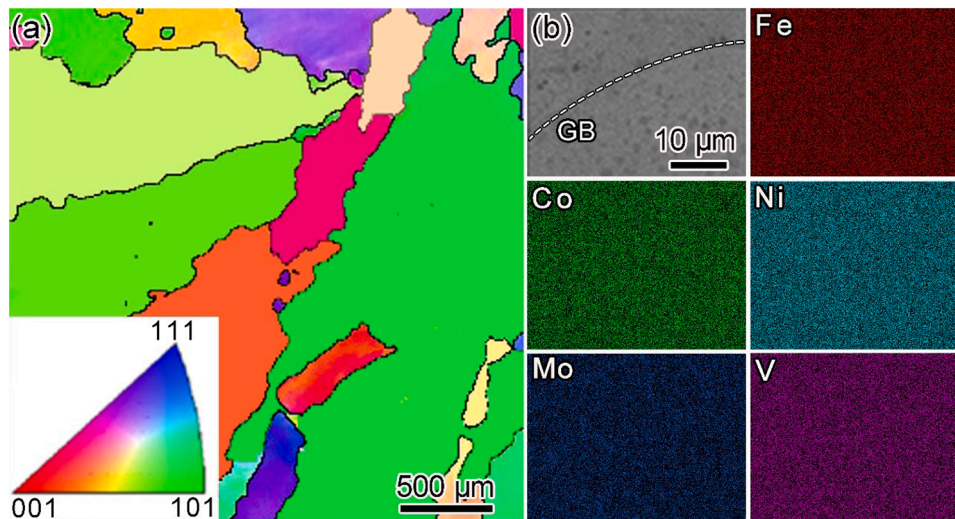


Fig. 1. Microstructures and compositional distributions of the as-annealed $\text{Ni}_2\text{Co}_1\text{Fe}_1\text{V}_{0.5}\text{Mo}_{0.2}$ MEA sample prior to creep tests. (a) An EBSD crystal orientation map showing millimeter-scale grains (the inset is the Inverse Pole Figure color code). (b) SEM-EDS maps showing homogeneous distributions of Ni, Co, Fe, V and Mo elements in the MEA.

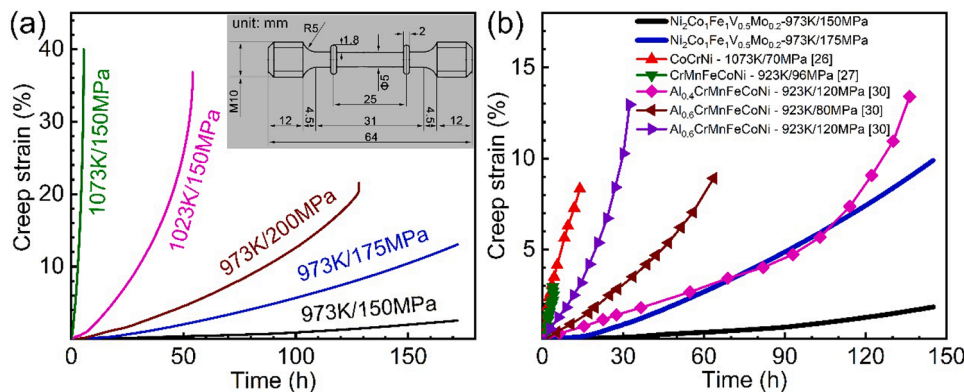


Fig. 2. (a) Creep strain (ϵ) vs. time (t) plots for the $\text{Ni}_2\text{Co}_1\text{Fe}_1\text{V}_{0.5}\text{Mo}_{0.2}$ MEA tested under the applied stresses 150–200 MPa, and at the temperatures 973–1073 K. The inset is a schematic drawing of the creep test specimen. (b) Comparison for tensile creep properties of some MEAs and HEAs [26,27,30].

three-stage creep curve in which the primary creep stage, steady-state creep stage and tertiary stage are readily distinctive. All of the creep strain – time curves for the $\text{Ni}_2\text{Co}_1\text{Fe}_1\text{V}_{0.5}\text{Mo}_{0.2}$ MEA are slightly concaved down, indicating the continuous increase in creep rate. The primary creep of the $\text{Ni}_2\text{Co}_1\text{Fe}_1\text{V}_{0.5}\text{Mo}_{0.2}$ MEA demonstrates inverse transient curves in Fig. 2a. Instead of having a steady-state creep stage, each creep strain – time curve shows only one inflection point beyond which the creep rate tends to increase faster, as shown in Fig. 3. Therefore, creep deformation for the $\text{Ni}_2\text{Co}_1\text{Fe}_1\text{V}_{0.5}\text{Mo}_{0.2}$ MEA has only the primary creep stage from the initiation of creep to the inflection point and the combined steady-state creep and tertiary creep stage from the inflection point to rupture [56]. The primary creep stage matches well with the classical description of power-law creep [45,57], but the usually long-lasting steady-state creep stage is undistinguishable from the tertiary creep stage as shown in Figs. 2a and 3. In order to determine a mechanical steady-state, the idea of the inflection point has been adopted from the work by Kassner and Perez-Prado [45]; Hence, the inflection point is now considered the transient secondary creep stage for the continuous transition from primary creep to the tertiary creep. Overall, the creep behavior of the $\text{Ni}_2\text{Co}_1\text{Fe}_1\text{V}_{0.5}\text{Mo}_{0.2}$ MEA resembles that of the Class I solid solution alloys, such as Al-Mg and Al-Zn alloys [57]. Thus, viscous-glide of dislocations and solute drag effect play critical roles in affecting the creep properties [45,58–60].

The steady-state creep rate of the $\text{Ni}_2\text{Co}_1\text{Fe}_1\text{V}_{0.5}\text{Mo}_{0.2}$ MEA can be

evaluated by the Arrhenius-type equation [61]:

$$\dot{\epsilon}_{\text{steady-state}} = A\sigma^n \exp\left(-\frac{Q}{RT}\right) \quad (1)$$

where A is a materials dependent constant, σ is the applied stress, n is the stress exponent, Q is the activation energy for creep deformation, R is the gas constant, and T is the absolute temperature. Since the $\text{Ni}_2\text{Co}_1\text{Fe}_1\text{V}_{0.5}\text{Mo}_{0.2}$ MEA has only a transient secondary creep stage, the creep strain rate at the inflection point is now considered the steady-state creep rate. Table 1 gives the time, strain and steady-state creep rates $\dot{\epsilon}$, at the inflection points, under different creep conditions for the $\text{Ni}_2\text{Co}_1\text{Fe}_1\text{V}_{0.5}\text{Mo}_{0.2}$ MEA. When the creep temperature is kept constant at 973 K, increase of the applied stress from 150 to 200 MPa leads to earlier inflection points and the increase of $\dot{\epsilon}$ from 1.90×10^{-8} to 4.69×10^{-8} . When the applied stress is kept to a constant of 150 MPa, temperature increase from 973 K to 1073 K leads to significantly shortened primary creep period and the drastic increase of $\dot{\epsilon}$ from 1.90×10^{-8} to 3.88×10^{-6} .

Based on Eq. (1), the relationship between the steady-state creep rate and the applied stress can be demonstrated by a log-log plot as shown in Fig. 4a. The stress exponent of $n \sim 3.1$ at 973 K is calculated by finding the slope of linear fitting to the data points in the plot. The reader is referred to Table S2 in the Supplementary material for the calculation of

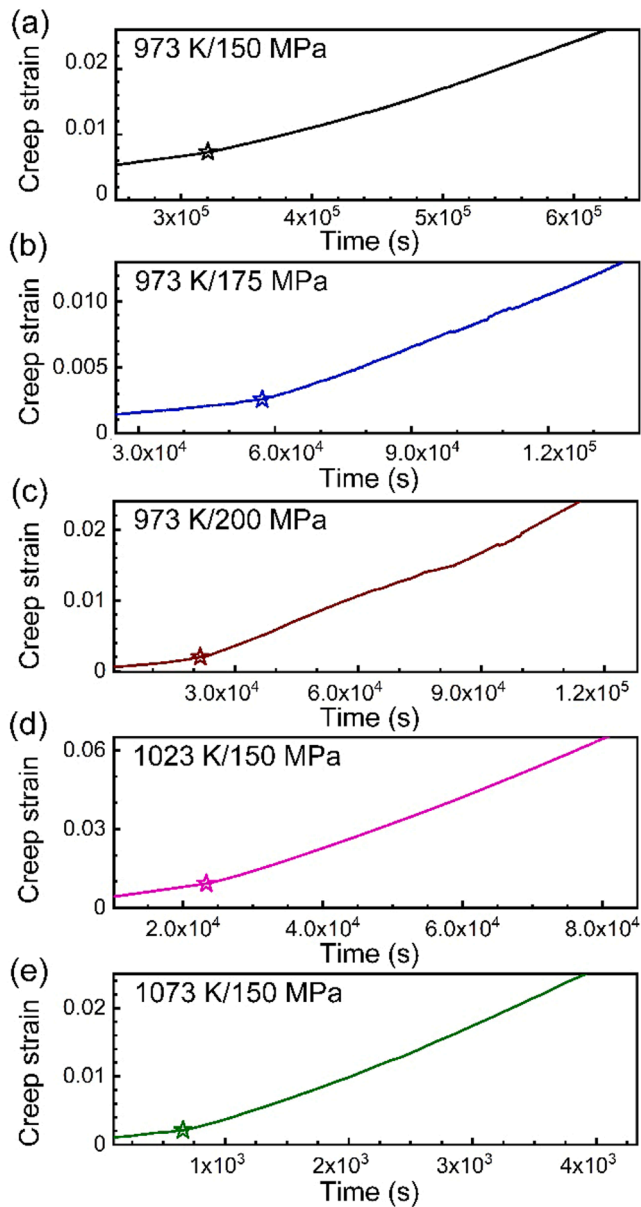


Fig. 3. Enlarged creep strain vs. time curves for the $\text{Ni}_2\text{Co}_1\text{Fe}_1\text{V}_{0.5}\text{Mo}_{0.2}$ MEA under the test conditions of (a) 973 K/150 MPa, (b) 973 K/175 MPa, (c) 973 K/200 MPa, (d) 1023 K/150 MPa, and (e) 1073 K/150 MPa.

Table 1

A list of time, strain and steady-state creep rates at the inflection points for the $\text{Ni}_2\text{Co}_1\text{Fe}_1\text{V}_{0.5}\text{Mo}_{0.2}$ MEA at different creep conditions.

Temperature (K)	973	973	973	1023	1073
Applied stress (MPa)	150	175	200	150	150
Time (h)	87.8	15.9	6.35	6.48	0.18
Strain (%)	0.72	0.26	0.22	0.92	0.2
Steady-state rate $\dot{\epsilon}$	1.90×10^{-8}	2.72×10^{-8}	4.69×10^{-8}	3.47×10^{-7}	3.88×10^{-6}

the stress exponent. The temperature dependence of the steady-state creep rate for the MEA is presented in Fig. 4b. Again, based on Eq. (1) and the linear correlation between the natural logarithm of the steady-state creep rates and the reciprocal of the absolute temperatures, the activation energy for steady-state creep is estimated to be $456.3 \text{ kJ}\cdot\text{mol}^{-1}$.

3.3. Creep mechanisms

Postmortem TEM analysis was performed to reveal the immanent deformation mechanisms governing creep deformation of the $\text{Ni}_2\text{Co}_1\text{Fe}_1\text{V}_{0.5}\text{Mo}_{0.2}$ MEA under different temperatures and applied stresses. Fig. 5 displays bright-field (BF) TEM micrographs and the corresponding selected area electron diffraction (SAED) patterns for the sample crept at 973 K and under the applied stress of 150 MPa. As shown in Fig. 5a, many long and straight dislocations lay parallel to $(\bar{1}11)$ and $(\bar{1}\bar{1}\bar{1})$ slip planes, suggesting that planar dislocation slip is strongly confined on $\{111\}$ planes. Careful TEM analysis revealed dislocation dipoles and SFs, as shown in Fig. 5b and c. A dipole is a pair of planar dislocations with opposite Burgers vectors laying on parallel slip planes. In fcc crystals, dipoles always lay on the most densely packed $\{111\}$ planes, but tend to line up along $\langle 211 \rangle$ directions [62]. For example, as shown in Fig. 5b, there is one group of dipoles, which are traced by horizontal red lines, laying on $(1\bar{1}\bar{1})$ planes. There are other groups of dipoles laying on $(\bar{1}\bar{1}\bar{1})$ or (111) planes and along $\langle 211 \rangle$ directions, as shown in Fig. 5b and d; In this case, the direction of the dipoles alignment, traced by red lines, shows an inclination of $\sim 80^\circ$ to the white $(\bar{1}\bar{1}\bar{1})$ trace line. Despite pronounced planar slip activities, dislocation interactions associated with cross slip and climb also occurred, evidenced by the curved dislocation lines that are unparallel to the $\{111\}$ slip planes, as shown in Fig. 5a and d. The coexistence of confined planar slip and cross slip is attributed to the high densities of dislocations and vacancies [14], and Suzuki segregation [63].

The samples crept under the constant stress of 175 MPa have random distributions of curved dislocations, as shown in Fig. 6a and b. Curved and looped dislocations marked by yellow arrows suggest cross slip and/or climb activities. There are also many dislocations with the cusped configuration which resembles a "knot" in shape with bowed dislocation segments on both sides (marked by green arrows). The formation of the cusped configuration is usually associated with jogs on screw dislocations [64]; in this case, the jog lays on a $\{111\}$ plane inclined to the slip plane of the screw dislocation, resulting in the unique dislocation line knot which is easily recognizable under diffraction contrast TEM imaging. The dislocation structures observed in the 973 K/200 MPa samples are similar to those in the 973 K/175 MPa samples. As shown in Fig. 6c, dislocation loops and jogs are abundant, and a sequence of dislocation loops of different sizes are traced by a pair of parallel yellow dotted lines. Some screw dislocations, which underwent cross slip, are marked by black arrows in Fig. 6d. Apparently, cross slip and climb activities are vigorous when the applied stress is above 175 MPa at the temperature of 973 K.

As shown in Fig. 7a, dislocations tangled and reorganized to form dislocation cells and sub-grains at 1023 K, indicating the occurrence of recovery and recrystallisation. Fig. 7b is a magnified TEM image showing typical dislocation cells with thick cell walls. While many dislocations have been pinned to the cell walls and other types of boundaries, the dislocation densities at grain interiors are significantly lower than that at boundaries. The sample crept at 1073 K shows similar microstructures to the one crept at 1023 K. As shown in Fig. 7c, sub-grains with sizes of a few micrometers are delineated by sharp boundaries. Provided that the sample prior to creep had grain sizes in the millimeter-scale, creep deformation induced grain refinement is evident. Fig. 7d is a magnified TEM image showing the intermediate stage for a dislocation cell transforming to a sub-grain. Letters A, B and C mark three dislocations pinned to the cell wall. At the bottom of the cell wall, there is a planar array of dislocations blocked by the wall. The cell wall is thick, but effective in trapping dislocations. In accordance to the conventional grain refinement process, as plastic deformation proceeds, a large number of dislocations will be absorbed by the thick cell wall, and eventually the cell wall will transform to a sharp sub-grain boundary [65]. The 973 K/150 MPa, 973 K/175 MPa and 973 K/200 MPa samples experienced the tensile strains ~ 2.4 , ~ 12.5 and ~ 21.6 , respectively;

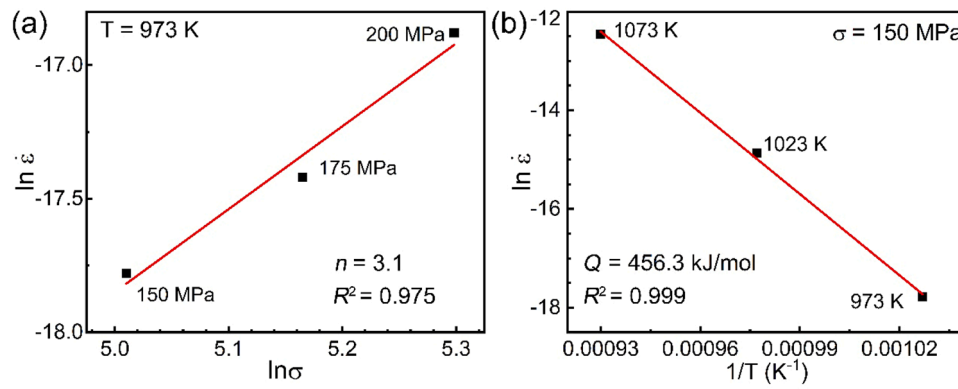


Fig. 4. (a) Natural logarithm plot of the steady-state creep rate vs. applied stress for the $\text{Ni}_2\text{Co}_1\text{Fe}_1\text{V}_{0.5}\text{Mo}_{0.2}$ MEA crept at 973 K. (b) A natural logarithm of steady-state creep rate vs. the reciprocal of absolute temperature plot for the sample crept under a constant stress of 150 MPa.

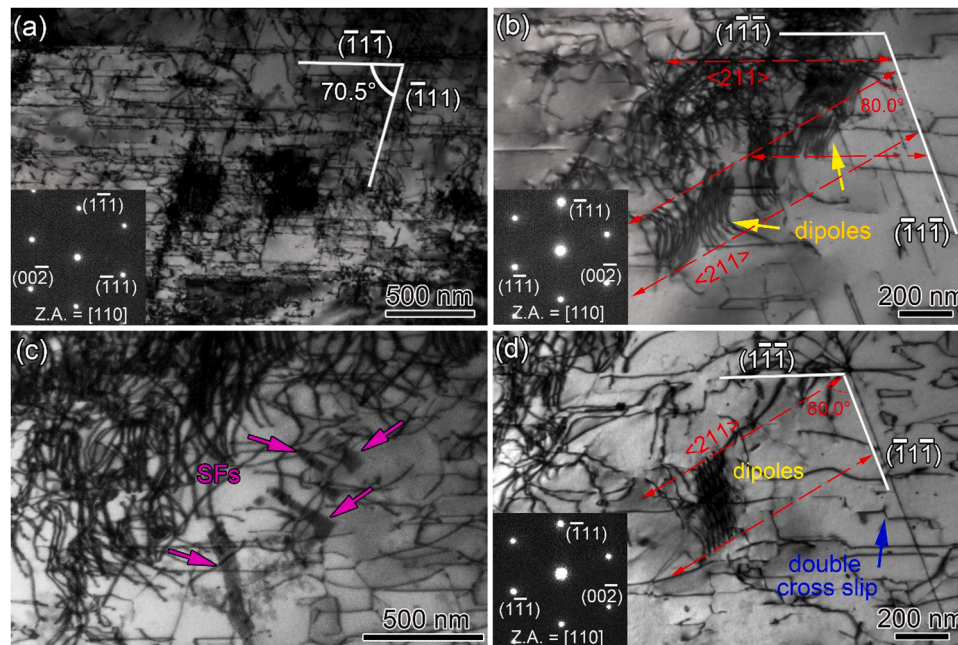


Fig. 5. TEM micrographs obtained near the $[110]$ zone axis, showing the microstructures in the $\text{Ni}_2\text{Co}_1\text{Fe}_1\text{V}_{0.5}\text{Mo}_{0.2}$ MEA crept at 973 K/150 MPa. (a) Planar slip character verified by the trace of dislocations laying on the $(\bar{1}\bar{1}\bar{1})$ and $(\bar{1}\bar{1}\bar{1})$ slip planes; (b) Tangled dislocations and dipoles; (c) Stacking faults; (d) Dislocation dipoles and double cross slip.

Figs. 5 and 6 show that grain refinement was not achieved when the stress was increased from 150 MPa to 200 MPa and the strain was increased from ~ 2.4 to ~ 21.6 . As shown in Fig. 7, grain refinement is evident in both 1023 K/150 MPa and 1073 K/150 MPa samples which have experienced tensile strains ~ 36.8 and ~ 39.9 , respectively. The 1023 K/150 MPa and 1073 K/150 MPa samples experienced higher temperatures and strains than the 973 K/150 MPa, 973 K/175 MPa and 973 K/200 MPa samples; Thus, it is concluded that increased temperature and strain are the driving factors for recovery, recrystallisation and the resultant grain refinement [66].

Based on the TEM analysis results, the effects of stress and strain on dislocation configurations can be summarized as follows: (1) As the stress increased from 150 to 200 MPa, the dominant microstructures changed from easy slip configurations such as planar screw, dipoles and SFs to less mobile configurations such as jogs and loops; (2) As the strain increased from ~ 21.6 to ~ 36.8 , the majority of dislocations are trapped in places to form low energy dislocation configurations such as forests, walls, and diffused low angle boundaries [65,67–69]. Detailed explanations on the formation of some specific dislocation configurations are

provided in the discussion section.

3.4. Fracture morphologies

Detailed SEM analysis was carried out to study the fracture modes for 973 K/200 MPa, 1023 K/150 MPa and 1073 K/150 MPa samples. As shown in Fig. 8a-1 and a-2, numerous globules are observed on the fracture surface, indicating the occurrence of ductile fracture for the 973 K/200 MPa sample. These globules formed due to partial melting and oxidation of the debris at the exposure of the fracture tip [44]. When the creep temperature is increased to 1023 K, the globules become more spherical than these found on the 973 K/200 MPa sample, as shown in Fig. 8b-1 and b-2. The average size of the globules observed on the fracture tip of the 1023 K/150 MPa sample is ~ 4.3 μm . When the creep temperature was increased to 1073 K, the average size of the globules formed on the fracture surface increased significantly to ~ 15.5 μm , as shown in Fig. 8c-1 and c-2. The average size of the globules was estimated by taking the mode of the statistical distribution of globule diameters. At least 200 globules have been measured from more than ten

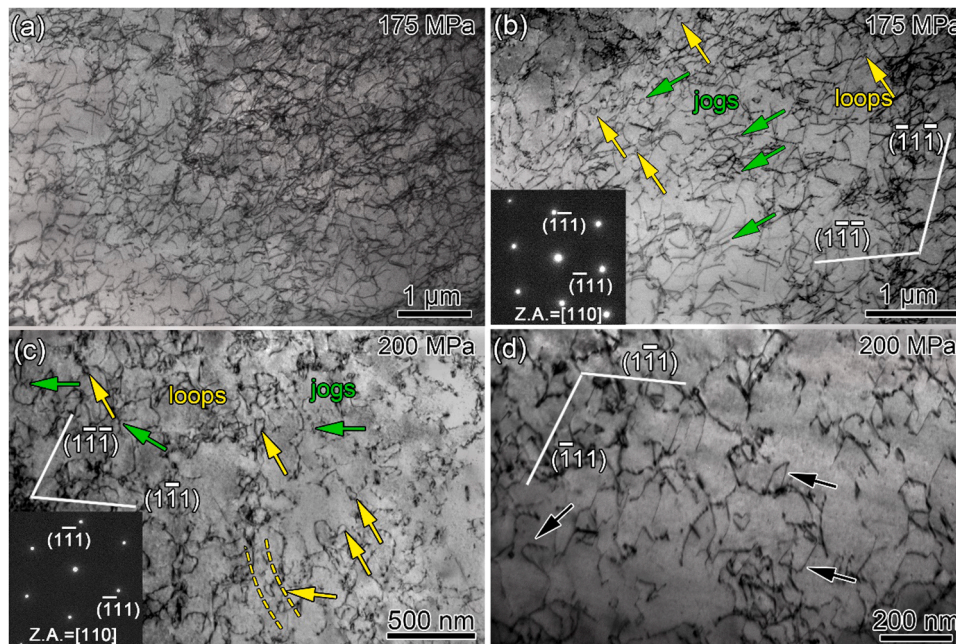


Fig. 6. TEM micrographs obtained near the [110] zone axis showing dislocation structures in the creep deformed $\text{Ni}_2\text{Co}_1\text{Fe}_1\text{V}_{0.5}\text{Mo}_{0.2}$ MEA samples: (a) and (b) 973 K/175 MPa sample; (c) and (d) 973 K/200 MPa sample. Green and yellow arrows mark dislocation jogs and loops, respectively. Black arrows mark dislocations underwent cross slip.

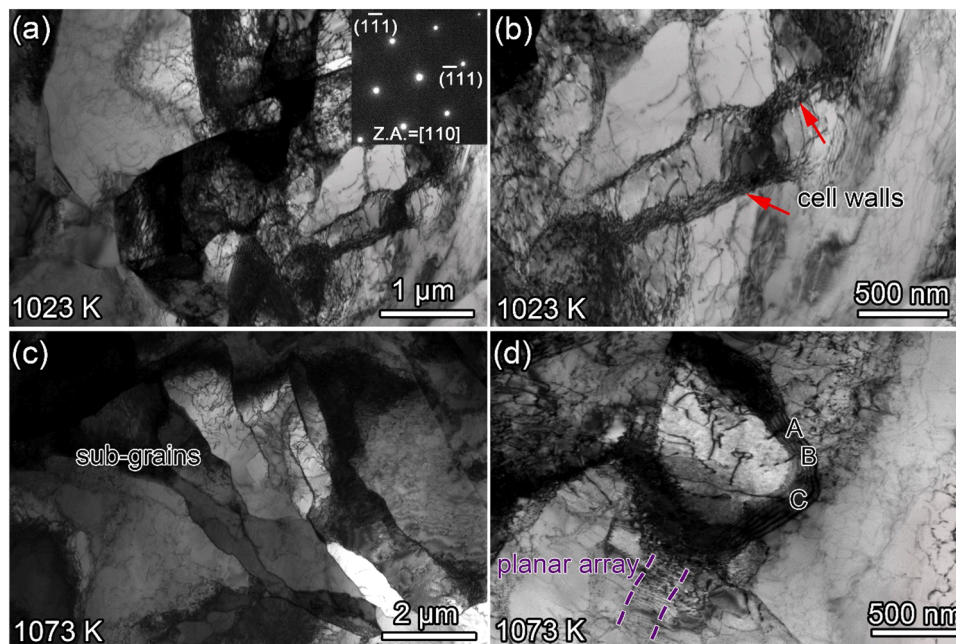


Fig. 7. TEM micrographs showing microstructures in the creep deformed $\text{Ni}_2\text{Co}_1\text{Fe}_1\text{V}_{0.5}\text{Mo}_{0.2}$ MEA samples: (a) and (b) substructures and dislocation cells in the 1023 K/150 MPa sample; (c) and (d) sub-grains, dislocation cells and planar arrays in the 1073 K/150 MPa sample. Letters A, B and C mark three dislocations pinned to the cell wall.

SEM images for each set of statistical analysis. The reader is referred to Fig. S1 and the corresponding description for the globule sizes measurement in the Supplementary material. It is worth noting that cleavage planes can be seen on the fracture surface of the 973 K/200 MPa as shown in Fig. 8a-1 and a-2. In contrast, the fracture surfaces of the 1023 K/150 MPa and 1073 K/150 MPa samples are covered completely by well-developed globules. Considering that the fracture stress for the 973 K/200 MPa sample is much higher than that for the 1023 K/150 MPa and 1073 K/150 MPa samples, stress plays a very minor role on the

development of globules, and meanwhile the crystalline structure of the $\text{Ni}_2\text{Co}_1\text{Fe}_1\text{V}_{0.5}\text{Mo}_{0.2}$ MEA is very stable at 973 K.

4. Discussion

4.1. Creep behavior and deformation mechanisms

Inverse primary creep for which creep strain rate increases with time is the characteristic creep behavior of Class I alloys, such as Al-Mg and

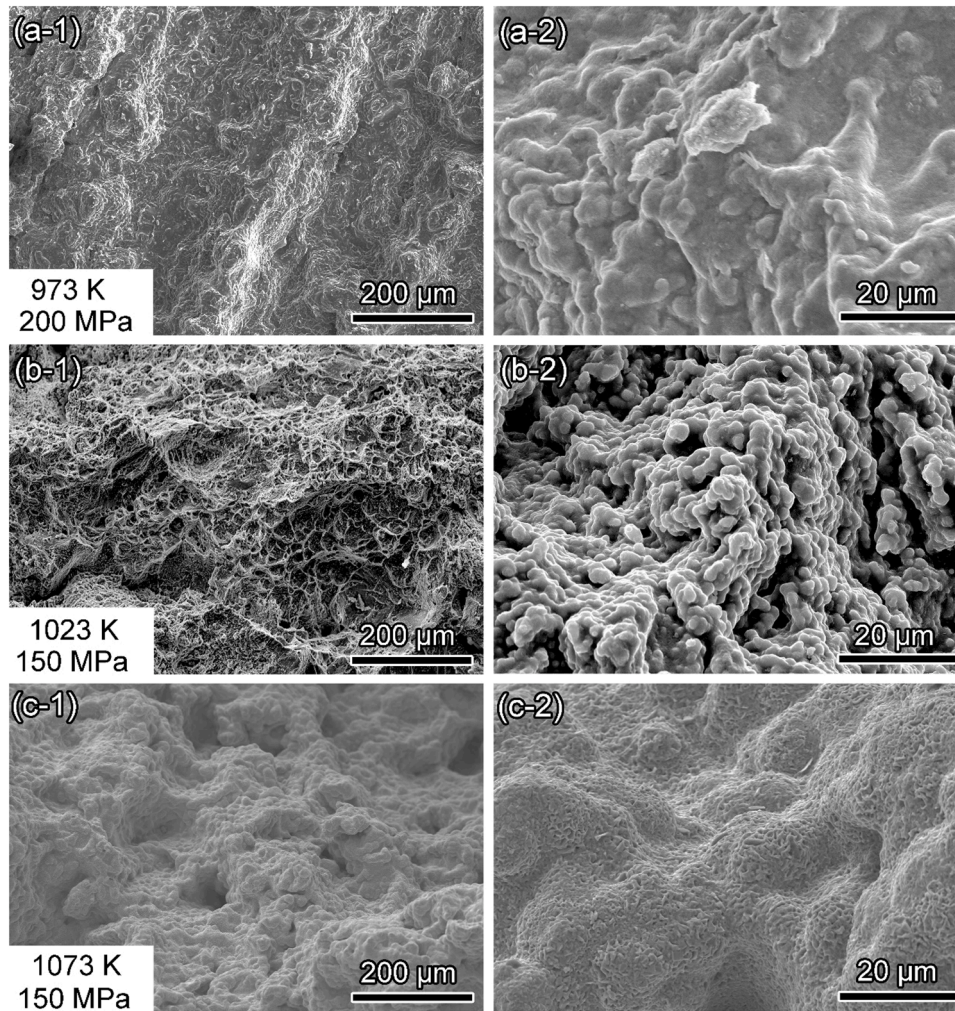


Fig. 8. SEM images showing fracture morphologies from the ruptured samples: (a-1) and (a-2) cleavage planes on the 973 K/200 MPa sample; (b-1) and (b-2) dimples and globules on the 1023 K/150 MPa sample; (c-1) and (c-2) globules on the 1073 K/150 MPa sample.

Al-Zn alloys with high solute contents and large atomic size misfits [70, 71]. Viscous glide of dislocations and sluggish development of sub-grains (Figs. 5 and 6) lead to the inverse primary creep of the $\text{Ni}_2\text{Co}_1\text{Fe}_1\text{V}_{0.5}\text{Mo}_{0.2}$ MEA, and thus making it a member of the Class I alloys family. Without effective development of sub-grains, the creep resistance is mainly attributed to solute pinning/drag on dislocations, entanglement of statistical dislocations at grain interiors, and impediment to dislocation slip by pre-existing grain boundaries [72,73]. At the ends of the primary creep stages which are the inflection points shown in Fig. 3, creep rates begin to increase faster due to increased tendency for dislocation climb and recovery, sustained viscous glide of dislocations and still sluggish development of sub-grains [45,74]. According to literatures [45,73,75,76], in order to have a steady-state creep stage at which strain hardening is balanced by dynamic recovery, dislocation generation has to be balanced by dislocation annihilation. To create the balance, a sufficient amount of sub-grain boundaries is necessary for following reasons [45]: (1) dislocation climb and annihilation mainly occur at the vicinities of sub-grain boundaries; (2) dislocations can pile up at a sub-grain boundary to create a long-range back-stress to “shuts off” the Frank-Read source; (3) the Frank-Read source is re-activated for dislocation emission, only if some of the dislocations within a given pile-up are annihilated at the sub-grain boundary to lower the back-stress. For creep of the $\text{Ni}_2\text{Co}_1\text{Fe}_1\text{V}_{0.5}\text{Mo}_{0.2}$ MEA governed by viscous glide of dislocations, sub-grains form only at the strain level close to the fracture strain, by then strain hardening has already been

overwhelmed by recovery and very possibly by cavitation [45,60]. Therefore, the steady-state creep stage is omitted for the creep of $\text{Ni}_2\text{Co}_1\text{Fe}_1\text{V}_{0.5}\text{Mo}_{0.2}$ MEA. In absence of the steady-state creep stage, the stress exponent of ~ 3.1 is estimated for the $\text{Ni}_2\text{Co}_1\text{Fe}_1\text{V}_{0.5}\text{Mo}_{0.2}$ MEA based on the creep rates at the inflection points, as shown in Fig. 4a, indicating the three power-law creep of the $\text{Ni}_2\text{Co}_1\text{Fe}_1\text{V}_{0.5}\text{Mo}_{0.2}$ MEA.

Since climb and viscous glide always occur in a solid solution alloy regardless which process is rate-controlling, in order to predict the rate-controlling mechanism, Mohamed and Langdon formulated a criterion for creep by viscous dislocation glide [74]:

$$\frac{B\sigma^2}{k^2(1-\nu)}\left(\frac{\gamma}{Gb}\right)^3 > \frac{T^2}{e^2cb^6} \quad (2)$$

where $B \sim 8 \times 10^{12}$, σ is the applied stress, k is Boltzmann's constant, ν is Poisson's ratio, γ is the SFE, G is the shear modulus, b is the Burgers vector, T is the absolute temperature, e is the solute-solvent size difference, and c is the concentration of solute atoms. Eq. (2) incorporates three important factors in determining the creep behavior: stress, temperature and solid solution. In the following subsections, the effects of the three factors on deformation mechanisms and resulting creep behaviors will be discussed.

4.2. Stress dependence

According to Eq. (1) and literatures [45,60,74], the creep rate is less

sensitive to stress under three power-law creep than that under five power-law creep, which suggests that Class I alloys are better creep resistant than pure metals and Class M alloys [60]. This statement is applicable to the $\text{Ni}_2\text{Co}_1\text{Fe}_1\text{V}_{0.5}\text{Mo}_{0.2}$ MEA studied here as well. According to Table 1, as the applied stress increased from 150 to 200 MPa, while the temperature was kept at 973 K, the steady-state creep rate increased moderately from 1.90×10^{-8} to 4.69×10^{-8} . Correspondingly, as shown in Fig. 3, the 973 K/150 MPa sample has the inflection point located at 87.8 h and 0.72% strain, but in contrast the 973 K/200 MPa sample has the inflection point located at 6.35 h and 0.22% strain, confirming that increased stress stimulates earlier ending of primary creep stage.

According to TEM analysis as shown in Figs. 5 and 6, the rate-controlling mechanism is still viscous dislocation glide despite of the increase of applied stress from 150 to 200 MPa. However, the dislocation configurations have changed conspicuously from planar dislocation dominance with random dislocation entanglements (Fig. 5) to homogeneous scattering of curved dislocations (Fig. 6), suggesting increased cross slip and climb activities with increasing stress [25,77–79]. This finding seems contradictory to Eq. (2) which indicates that increasing stress promotes viscous dislocation glide over dislocation climb [74].

The explanation for the contradiction is rather complex, because of the many factors and mechanisms involved in creep deformation. First of all, dislocation emission and glide are driven by stress; therefore, stress promotes viscous dislocation glide. However, if there are high densities of vacancies in the bulk material, a large number of dislocations will unavoidably interact with vacancies during slip, leading to active dislocation climb, and in this case the high stress may even promote the dislocation-vacancy interaction by promoting slip activities. Therefore, a high density of vacancies is in fact the key factor for enhanced dislocation climb, and the stress effect on climb is rather indirect and case dependent.

Introduction of a vacancy will increase the free energy of the bulk crystalline solid by Δg_f which is called the free energy of vacancy formation. It can be expressed as [80]:

$$\Delta g_f = \Delta h_f - T\Delta s_f = \Delta e_f + P\Delta v_f - T\Delta s_f \quad (3)$$

where Δh_f and Δs_f are the enthalpy and entropy of formation, respectively; Δe_f is the formation energy of a vacancy, Δv_f is the formation volume of a vacancy, and P is the external pressure. Δv_f is theoretically one atomic volume if no relaxation occurs, but in reality it is somewhat smaller by 10 to 40%. Under normal conditions the $P\Delta v_f$ term is several orders of magnitude smaller than Δe_f . Therefore, Δh_f and Δe_f are practically equal to each other. The vacancy formation enthalpy in fcc metals is known to be correlated with the melting temperature T_m and thus expressed as:

$$\Delta h_f \approx 10kT_m \quad (4)$$

The formation entropy Δs_f is commonly 1–2 times k . By using Eq. (4), the formation energy Δe_f of a vacancy at 973 K is estimated to be 1.45 eV. Correspondingly, the free energy Δg_f of vacancy formation is calculated to be 1.29–1.37 eV, by substituting the estimated values of Δe_f and Δs_f into Eq. (3).

In practice, the number of vacancies, n , is orders of magnitude smaller than the number of atoms, N , in bulk crystalline materials, and thus interactions between vacancies are ignored in analysis. Then, the total change in the free energy is given by:

$$\Delta G = n\Delta g_f - TS_c \quad (5)$$

where S_c is the configurational entropy. Under the equilibrium condition $\frac{\partial \Delta G}{\partial n} = 0$, the equilibrium concentration of vacancies can be expressed as [80]:

$$c = \frac{n}{n+N} = \exp\left(-\frac{\Delta g_f}{kT}\right) \quad (6)$$

By using Eq. (6), the equilibrium concentration of vacancies at 973 K is calculated to be $8.25 \times 10^{-8} \sim 2.17 \times 10^{-7}$. However, vacancies generation and annihilation during high temperature creep deformation (under continuous input of strain energy) are a dynamic process, so the instantaneous concentration of vacancies shall be even higher than the equilibrium concentration. However, the next question comes that where the excess vacancies come from, when the creep temperature is kept to a constant? In examining the characteristic microstructures shown in Fig. 6, we propose that the excess vacancies are created by the jog dragging process describe as below:

- (1) Gliding dislocations on intersected planes can intersect each other as the plastic deformation proceeds. Intersecting of dislocations left jogs (steps) on a screw dislocation as illustrated in Fig. 9a.
- (2) Under the local shear stress acting on the slip plane in the direction of the Burgers vector b , the dislocation bows out between the jogs; Bowing of the dislocation draws out a dislocation dipole consisting of two edge components of opposite sign, as shown in Fig. 9b.
- (3) The screw dislocation can move forward and pull the jogs with it, only by a non-conservative process. The non-conservative process requires net loss or gain of vacancies or self-interstitial atoms. Under the effects of strain and thermal activation, vacancies may actively diffuse and coalesce to the moving jogs, provided that a jog can be a source and sink for vacancies. The dipole on the jog may break up because of the mutual attraction of the positive and negative edge components at the two elongated sides, to form a vacancy loop behind, as shown in Fig. 9c.
- (4) Continuous movement of the screw dislocation with jogs will leave behind trails of vacancy loops, as shown in Fig. 9d. Theoretically speaking, the jog dragging process can create either a trail of vacancies or interstitial atoms, depending on the sign and direction of the moving dislocation. However, the formation energy of a self-interstitial is typically two to four times the formation energy Δe_f of a vacancy, so the production of self-interstitial atoms is rare [81]. Since thermal diffusion of vacancies is energetically favored during high temperature creep, sequences of vacancy loops are easily formed by the randomly occurring jog dragging process, as revealed in Fig. 6c.

Both jog and vacancy loop are sources of vacancies [45]. Vacancies, jogs and loops may interact with dislocations to cause climb [29,82]. For example, a pure screw dislocation has no extra half-plane and thus in principle cannot climb; However, a jog on a screw dislocation can provide a site for the climb activity. For another example, a straight dislocation with a screw component can climb by interacting with a loop, and transform into a curved dislocation; the curved dislocation can continue climb under shear stress to form a helical dislocation [82]. To sum up, the homogeneous scattering of curved dislocations as shown in Fig. 6 is formed by active cross slip and climb. The major driving factor for the climb activity is the excess vacancies created by the jog dragging process. The jog dragging process is initiated by stress-driven dislocation interactions. The increased stress is still the major driving factor for viscous dislocation glide, but may indirectly promote dislocation climb. Nevertheless, the creep rate-controlling mechanism is still viscous dislocation glide when the applied stress was increased to 175 and 200 MPa, despite of enhanced climb activities and moderately increased creep rates.

4.3. Temperature dependence

According to Eq. (2), the rate-controlling mechanism may shift towards dislocation climb at high temperatures, evidenced by the formation of dislocation cells and sub-grains (Fig. 7) [83,84], and significantly increased steady state creep rates (Table 1) at 1023 K and 1073 K.

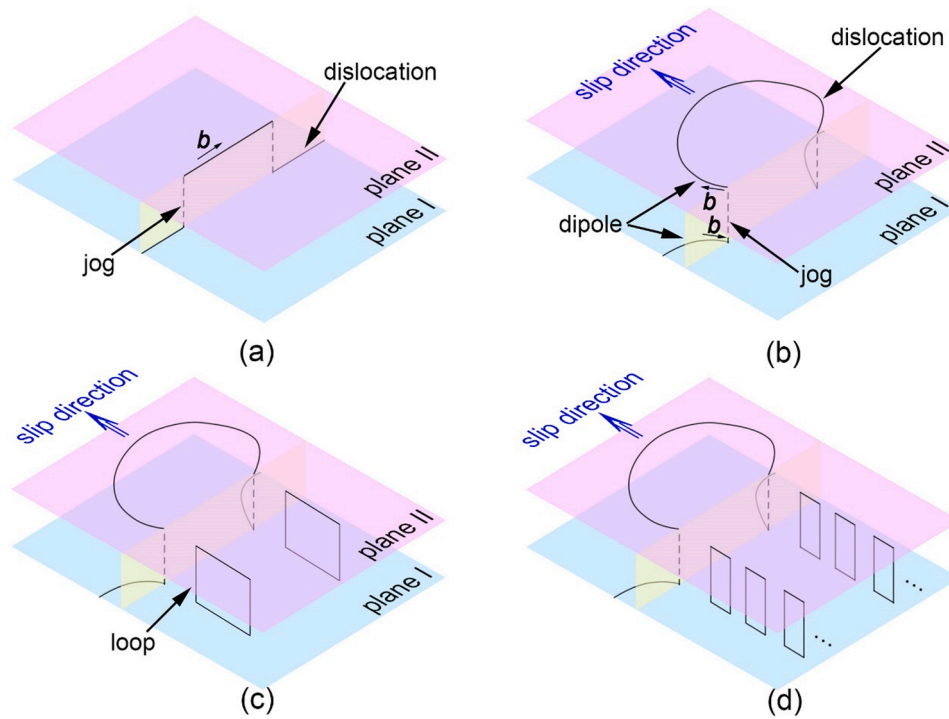


Fig. 9. Schematic illustration of the jog dragging process. (a) Jogs form on a screw dislocation; (b) The pinned dislocation bows out to create dipoles at the pinning jogs; (c) The screw dislocation moves forward and drags the jogs with it, while creating loops on the path; (d) Gliding of the jogged screw dislocation produces trails of loops.

Correspondingly, as shown in Fig. 3, the 973 K/150 MPa sample has the inflection point located at 87.8 h and 0.72% strain, but in contrast the 1073 K/150 MPa sample has the inflection point located at 0.18 h and 0.2% strain, indicating that increased temperature also stimulates earlier ending of primary creep stage.

The elongated sub-grains shown in Fig. 7c are an indication of diffusional creep, by which the atomic movements and vacancies migration cause the grains to extend along the tensile axis and shrink vertically during deformation. The activation energy for defects migration decreases with increasing temperature, therefore the rate of vacancies diffusion increases to promote dislocation climb, and the probability of cross slip increases to promote dislocation annihilation. Moreover, the SFE which directly affects dislocation configuration and cross slip, increases with increasing temperature [85,86]. At room temperature, the $\text{Ni}_2\text{Co}_1\text{Fe}_1\text{V}_{0.5}\text{Mo}_{0.2}$ MEA has an SFE of ~ 50 mJ/m² [25], which is comparable to that of a copper. Further increase in SFE due to elevated temperature confines the separation of partial dislocations to facilitate cross slip. Apparently, recovery and annihilation of dislocations are vigorous due to active cross slip and climb of dislocations, when the $\text{Ni}_2\text{Co}_1\text{Fe}_1\text{V}_{0.5}\text{Mo}_{0.2}$ MEA is crept at 1023 and 1073 K. However, the corresponding creep strain curves in Fig. 2 show no extended steady-state creep stage. The sub-grain structures shown in Fig. 7, have been observed at high strain levels close to the fracture strain. Thus, the grain refinement shown in Fig. 7 is a combined result of high creep temperature and high strain. Therefore, elevation of the creep temperature to 1023 and 1073 K has not changed the rate-controlling mechanisms (viscous dislocation glide is still in dominance), despite of significantly enhanced climb and cross slip activities.

4.4. Solid solution effect

According to the criterion for creep by viscous dislocation glide proposed by Mohamed and Langdon [74], the solid solution effect on deformation mechanisms and the resulting creep properties are attributed to the intrinsic material properties: solute concentration,

atomic-size mismatch, shear modulus and SFE (the SFE has been discussed in the previous subsection, so no further discussion is given hereafter). All MEAs and HEAs are concentrated solid solutions with sluggish lattice diffusion [87]. In the $\text{Ni}_2\text{Co}_1\text{Fe}_1\text{V}_{0.5}\text{Mo}_{0.2}$ MEA, the constituent elements possess very different atomic-size and shear modulus (Ni: $r = 1.21$ Å, $G = 80$ GPa; Fe: $r = 1.27$ Å, $G = 41.3$ GPa; Co: $r = 1.26$ Å, $G = 83$ GPa; V: $r = 1.35$ Å, $G = 47$ GPa; Mo: $r = 1.4$ Å, $G = 20$ GPa), inducing large atomic-size mismatch and elastic modulus mismatch [43]. The distorted local lattice due to atomic-size mismatch and elastic modulus mismatch produces short-range stress fields to hinder dislocation movement, resulting in the strong solute-pinning effect [43]. The strong solute-pinning effect improves the strength and creep resistance of alloys, but not necessarily guarantee the rate-controlling by viscous dislocation glide. According to Eq. (2), it is the large atomic size difference and reduced bulk shear modulus promote viscous dislocation glide.

For the $\text{Ni}_2\text{Co}_1\text{Fe}_1\text{V}_{0.5}\text{Mo}_{0.2}$ MEA, the constituent elements Mo and V possess much larger atomic radii than the other three elements. The average atomic size difference δ is expressed as [88]:

$$\delta = \sqrt{\sum_{i=1}^n x_i (1 - r_i/\bar{r})^2} \quad (7)$$

where r_i and x_i are the atomic radius and percentage of the i element, respectively, \bar{r} is the average atomic radius. According to Eq. (7), the average atomic size difference δ in the $\text{Ni}_2\text{Co}_1\text{Fe}_1\text{V}_{0.5}\text{Mo}_{0.2}$ MEA is calculated to be 0.0421, much larger than that of the CrMnFeCoNi HEA (0.0207).

The shear modulus of the $\text{Ni}_2\text{Co}_1\text{Fe}_1\text{V}_{0.5}\text{Mo}_{0.2}$ MEA is measured to be 43.5 GPa at 973 K, lower than that of the CrMnFeCoNi HEA (57.6 GPa) [89], CrFeCoNi MEA (61.6 GPa), CrCoNi MEA (67.2 GPa) [90], Ni-based superalloy René 88DT (60.6 GPa) [91,92] and Ni-based superalloy single crystal CMSX-4 (60–86.5 GPa, orientation dependent) [93]. To sum up, high solute concentration, large atomic size mismatch and low shear modulus work together to sustain viscous dislocation glide in

$\text{Ni}_2\text{Co}_1\text{Fe}_1\text{V}_{0.5}\text{Mo}_{0.2}$ MEA, even at very high temperatures up to 1073 K.

Mo and V are common alloying elements in alloys for high temperature applications, because of their high melting points and high activation energy for atomic diffusion [33,35–37,94]. As shown in Fig. 4b, the $\text{Ni}_2\text{Co}_1\text{Fe}_1\text{V}_{0.5}\text{Mo}_{0.2}$ MEA has an activation energy of $456.3 \text{ kJ}\cdot\text{mol}^{-1}$ for creep deformation, which is comparable to that of the CrFeCo-NiMo_{0.2} HEA ($463 \text{ kJ}\cdot\text{mol}^{-1}$) [85], stainless steel ($460 \text{ kJ}\cdot\text{mol}^{-1}$) [95] and nickel-based superalloys ($443 \text{ kJ}\cdot\text{mol}^{-1}$) [96]. It is noticed that the activation energy for lattice diffusion of Mo element is about $480 \text{ kJ}\cdot\text{mol}^{-1}$ [97–99], which is only slightly higher than the creep activation energy of the $\text{Ni}_2\text{Co}_1\text{Fe}_1\text{V}_{0.5}\text{Mo}_{0.2}$ MEA. This is because the jog sites are blocked by Mo, so that the power law creep rate of the MEA is depressed and the creep activation energy is risen [100]. In contrast, the creep activation energies for CoCrFeMnNi HEAs and AlxCrMnFeCoNi HEAs are only $284\text{--}333 \text{ kJ}\cdot\text{mol}^{-1}$ [101] and $258\text{--}349 \text{ kJ}\cdot\text{mol}^{-1}$ [30], respectively. Apparently, the creep activation energy of $\text{Ni}_2\text{Co}_1\text{Fe}_1\text{V}_{0.5}\text{Mo}_{0.2}$ MEA is very high among HEAs and MEAs. By comparing the activation energies among the aforementioned alloys, it is apparent that solid solution with V and Mo is beneficial for improving creep properties by limiting the rate of diffusion with a high activation energy. Especially, sluggish lattice diffusion of Mo in the current case may be the major cause of the high creep activation energy.

5. Conclusion

The creep properties and deformation mechanisms of the $\text{Ni}_2\text{Co}_1\text{Fe}_1\text{V}_{0.5}\text{Mo}_{0.2}$ MEA at high temperatures (973–1073 K) and under varied tensile stresses (150–200 MPa) have been investigated in detail. Based on systematic analysis and in-depth discussion, the following conclusions can be drawn:

- 1 The multi-principal element design with the addition of V and Mo grants the $\text{Ni}_2\text{Co}_1\text{Fe}_1\text{V}_{0.5}\text{Mo}_{0.2}$ MEA with outstanding creep resistance at 973 K/150 MPa. Increasing the applied stress increases moderately the steady-state creep rate due to early activation of jog dragging process. In contrast, increasing the temperature increases significantly the steady-state creep rate by strong promotion of cross slip and climb.
- 2 The stress exponent and the creep activation energy of the $\text{Ni}_2\text{Co}_1\text{Fe}_1\text{V}_{0.5}\text{Mo}_{0.2}$ MEA are calculated to be ~ 3.1 and $456.3 \text{ kJ}\cdot\text{mol}^{-1}$, respectively. The stress exponent of ~ 3 indicates the rate controlling mechanism of viscous dislocation glide. The activation energy for creep deformation is close to that of the lattice diffusion of Mo, indicating that sluggish diffusion of Mo has a strong effect on limiting the creep rate.
- 3 Under the low stress, low temperature and low strain condition, planar dislocations with random entanglements are the characteristic microstructure; Under the high stress, low temperature and low to medium strain condition, homogeneous scattering of curved dislocations are the characteristic microstructure; Under the low stress, high temperature and high strain condition, the sub-grain structures eventually form due to the strong recovery effect. Although dislocation configurations and microstructures change noticeably due to the promotion of cross slip and climb activities by increasing stress, temperature and strain, viscous dislocation glide sustains as the rate-controlling mechanism.

In summary, this work systematically evaluated the relationship between microstructural evolution and creep properties in a $\text{Ni}_2\text{Co}_1\text{Fe}_1\text{V}_{0.5}\text{Mo}_{0.2}$ MEA, and classified the MEA into the Class I alloys family. While the conventional Mohamed-Langdon criterion for creep by viscous dislocation glide is proven applicable to concentrated solid solutions such as the $\text{Ni}_2\text{Co}_1\text{Fe}_1\text{V}_{0.5}\text{Mo}_{0.2}$ MEA studied here, the stress effect on rate-controlling mechanisms requires a new understanding that high stress is the major driving factor for viscous dislocation glide, but

may indirectly promote dislocation climb. This is because the stress driven jog dragging process can be vigorously activated to create excess amounts of vacancies which in turn promote dislocation-vacancy interactions and thus dislocation climb. Nevertheless, our work also provides solid evidence that the materials design concept of adding V and Mo is feasible for improving creep properties by limiting the rate of diffusion with a high activation energy. Our result is readily to be used to guide future design of high temperature MEAs and HEAs.

Funding

This research is funded by the National Key R&D Program of China (Grant No. 2021YFA1200203), the National Natural Science Foundation of China (Grant Nos. 51971112 and 52071181), the Six Talent Peaks Project of Jiangsu Province (Grant No. 2017-XCL-051), and the Fundamental Research Funds for the Central Universities (Grant No. 30919011405 and 30917011106).

CRedit authorship contribution statement

Wei Jiang: Data curation, Visualization, Writing – original draft, Investigation. **Yang Cao:** Validation, Formal analysis, Funding acquisition. **Shengyun Yuan:** Investigation. **Yong Zhang:** Conceptualization, Supervision, Writing – review & editing, Validation, Formal analysis, Funding acquisition. **Yonghao Zhao:** Conceptualization, Supervision, Writing – review & editing, Funding acquisition.

Declaration of Competing Interest

The authors declare no conflict of interest.

Acknowledgments

The authors are thankful for the technical support from Jiangsu Key Laboratory of Advanced Micro&Nano Materials and Technology, and the Materials Characterization Facility of Nanjing University of Science and Technology.

Supplementary materials

Supplementary material associated with this article can be found, in the online version, at doi:[10.1016/j.actamat.2022.118590](https://doi.org/10.1016/j.actamat.2022.118590).

References

- [1] J.W. Yeh, S.K. Chen, S.J. Lin, J.Y. Gan, T.S. Chin, T.T. Shun, C.H. Tsau, S. Y. Chang, Nanostructured high-entropy alloys with multiple principal elements: novel alloy design concepts and outcomes, *Adv. Eng. Mater.* 6 (2004) 299–303.
- [2] B. Cantor, I.T.H. Chang, P. Knight, A.J.B. Vincent, Microstructural development in equiatomic multicomponent alloys, *Mater. Sci. Eng. A* 375–377 (2004) 213–218.
- [3] Y. Zhang, T.T. Zuo, Z. Tang, M.C. Gao, K.A. Dahmen, P.K. Liaw, Z.P. Lu, Microstructures and properties of high-entropy alloys, *Prog. Mater. Sci.* 61 (2014) 1–93.
- [4] Z.F. Lei, X.J. Liu, Y. Wu, H. Wang, S.H. Jiang, S.D. Wang, X.D. Hui, Y.D. Wu, B. Gault, P. Kontis, D. Raabe, L. Gu, Q.H. Zhang, H.W. Chen, H.T. Wang, J.B. Liu, K. An, Q.S. Zeng, T.G. Nieh, Z.P. Lu, Enhanced strength and ductility in a high-entropy alloy via ordered oxygen complexes, *Nature* 563 (2018) 546–550.
- [5] Z.M. Li, K.G. Pradeep, Y. Deng, D. Raabe, C.C. Tasan, Metastable high-entropy dual-phase alloys overcome the strength-ductility trade-off, *Nature* 534 (2016) 227–230.
- [6] B. Gludovatz, A. Hohenwarter, D. Catoor, E.H. Chang, E.P. George, R.O. Ritchie, A fracture-resistant high-entropy alloy for cryogenic applications, *Science* 345 (2014) 1153–1158.
- [7] G. Laplanche, A. Kostka, O.M. Horst, G. Eggeler, E.P. George, Microstructure evolution and critical stress for twinning in the CrMnFeCoNi high-entropy alloy, *Acta Mater.* 118 (2016) 152–163.
- [8] Y.Q. Wang, B. Liu, K. Yan, M.S. Wang, S. Kabra, Y.L. Chiu, D. Dye, P.D. Lee, Y. Liu, B. Cai, Probing deformation mechanisms of a FeCoCrNi high-entropy alloy at 293 and 77 K using in situ neutron diffraction, *Acta Mater.* 154 (2018) 79–89.

- [9] G. Laplanche, A. Kostka, C. Reinhart, J. Hunfeld, G. Eggeler, E.P. George, Reasons for the superior mechanical properties of medium-entropy CrCoNi compared to high-entropy CrMnFeCoNi, *Acta Mater.* 128 (2017) 292–303.
- [10] J. Moon, E. Tabachnikova, S. Shumilina, T. Hryhorova, Y. Estrin, J. Brechtel, P. K. Liaw, W. Wang, K.A. Dahmen, A. Zargarani, J.W. Bae, H.S. Do, B.J. Lee, H. S. Kim, Deformation behavior of a Co-Cr-Fe-Ni-Mo medium-entropy alloy at extremely low temperatures, *Mater. Today* 50 (2021) 55–68.
- [11] K.Y. Tsai, M.H. Tsai, J.W. Yeh, Sluggish diffusion in Co–Cr–Fe–Mn–Ni high-entropy alloys, *Acta Mater.* 61 (2013) 4887–4897.
- [12] H.Q. Song, F.Y. Tian, Q.M. Hu, L. Vitos, Y.D. Wang, J. Shen, N.X. Chen, Local lattice distortion in high-entropy alloys, *Phys. Rev. Mater.* 1 (2017), 023404.
- [13] X.F. Chen, Q. Wang, Z.Y. Cheng, M.L. Zhu, H. Zhou, P. Jiang, L.L. Zhou, Q.Q. Xue, F.P. Yuan, J. Zhu, X.L. Wu, E. Ma, Direct observation of chemical short-range order in a medium-entropy alloy, *Nature* 592 (2021) 712–716.
- [14] Q.Q. Ding, Y. Zhang, X. Chen, X.Q. Fu, D.K. Chen, S.J. Chen, L. Gu, F. Wei, H. B. Bei, Y.F. Gao, M.R. Wen, J.X. Li, Z. Zhang, T. Zhu, R.O. Ritchie, Q. Yu, Tuning element distribution, structure and properties by composition in high-entropy alloys, *Nature* 574 (2019) 223–227.
- [15] Q.J. Li, H. Sheng, E. Ma, Strengthening in multi-principal element alloys with local-chemical-order roughened dislocation pathways, *Nat. Commun.* 10 (2019) 3563.
- [16] S. Chen, Z.H. Aitken, S. Pattamatta, Z. Wu, Z.G. Yu, D.J. Srolovitz, P.K. Liaw, Y. W. Zhang, Simultaneously enhancing the ultimate strength and ductility of high-entropy alloys via short-range ordering, *Nat. Commun.* 12 (2021) 4953.
- [17] R.P. Zhang, S.T. Zhao, J. Ding, Y. Chong, T. Jia, C. Ophus, M. Asta, R.O. Ritchie, A.M. Minor, Short-range order and its impact on the CrCoNi medium-entropy alloy, *Nature* 581 (2020) 283–287.
- [18] H. Chang, T.W. Zhang, S.G. Ma, D. Zhao, R.L. Xiong, T. Wang, Z.Q. Li, Z.H. Wang, Novel Si-added CrCoNi medium entropy alloys achieving the breakthrough of strength-ductility trade-off, *Mater. Des.* 197 (2021), 109202.
- [19] S. Shukla, R.S. Mishra, Excellent high cyclic fatigue properties of a novel ultrafine-grained medium entropy alloy, *Mater. Sci. Eng. A* 779 (2020), 139122.
- [20] M.X. Yang, L.L. Zhou, C. Wang, P. Jiang, F.P. Yuan, E. Ma, X.L. Wu, High impact toughness of CrCoNi medium-entropy alloy at liquid-helium temperature, *Scr. Mater.* 172 (2019) 66–71.
- [21] W.D. Li, P.K. Liaw, Y.F. Gao, Fracture resistance of high entropy alloys: a review, *Intermetallics* 99 (2018) 69–83.
- [22] F. Otto, A. Dlouhý, C. Somsen, H. Bei, G. Eggeler, E.P. George, The influences of temperature and microstructure on the tensile properties of a CoCrFeMnNi high-entropy alloy, *Acta Mater.* 61 (2013) 5743–5755.
- [23] J.H. Kim, Y.S. Na, Tensile properties and serrated flow behavior of as-cast CoCrFeMnNi high-entropy alloy at room and elevated temperatures, *Met. Mater. Int.* 25 (2018) 296–303.
- [24] L.L. Han, X.D. Xu, Z.M. Li, B. Liu, C.T. Liu, Y. Liu, A novel equiaxed eutectic high-entropy alloy with excellent mechanical properties at elevated temperatures, *Mater. Res. Lett.* 8 (2020) 373–382.
- [25] L. Jiang, Y.P. Lu, M. Song, C. Lu, K. Sun, Z.Q. Cao, T.M. Wang, F. Gao, L.M. Wang, A promising CoFeNi₂V_{0.5}Mo_{0.2} high entropy alloy with exceptional ductility, *Scr. Mater.* 165 (2019) 128–133.
- [26] D. Xie, R. Feng, P.K. Liaw, H.B. Bei, Y.F. Gao, Tensile creep behavior of an equiatomic CoCrNi medium entropy alloy, *Intermetallics* 121 (2020), 106775.
- [27] Y.B. Kang, S.H. Shim, K.H. Lee, S.I. Hong, Dislocation creep behavior of CoCrFeMnNi high entropy alloy at intermediate temperatures, *Mater. Res. Lett.* 6 (2018) 689–695.
- [28] K.A. Rozman, M. Detrois, M.C. Gao, P.D. Jablonski, J.A. Hawk, Long-term creep behavior of a CoCrFeNi medium-entropy alloy, *J. Mater. Eng. Perform.* 31 (2022) 9220–9235.
- [29] C.M. Cao, J.X. Fu, T.W. Tong, Y.X. Hao, P. Gu, H. Hao, L.M. Peng, Intermediate-temperature creep deformation and microstructural evolution of an equiatomic FCC-structured CoCrFeNiMn high-entropy alloy, *Entropy* 20 (2018) 960.
- [30] C.M. Cao, J. Xu, W. Tong, Y.X. Hao, P. Gu, L.M. Peng, Creep behaviour and microstructural evolution of Al₃CrMnFeCoNi high-entropy alloys, *Mater. Sci. Technol.* 35 (2019) 1283–1290.
- [31] T.K. Tsao, A.C. Yeh, C.M. Kuo, K. Takehi, H. Murakami, J.W. Yeh, S.R. Jian, The high temperature tensile and creep behaviors of high entropy superalloy, *Sci. Rep.* 7 (2017) 12658.
- [32] G. Chen, Y.B. Peng, G. Zheng, Z.X. Qi, M.Z. Wang, H.C. Yu, C.L. Dong, C.T. Liu, Polysynthetic twinned TiAl single crystals for high-temperature applications, *Nat. Mater.* 15 (2016) 876–881.
- [33] F. Appel, M. Oehring, J.D.H. Paul, A novel *in situ* composite structure in TiAl alloys, *Mater. Sci. Eng. A* 493 (2008) 232–236.
- [34] H.X. Pei, S.X. Li, L.X. Wang, H.L. Zhang, Z.D. Zhao, X.T. Wang, Influence of initial microstructures on deformation behavior of 316LN austenitic steels at 400–900 °C, *J. Mater. Eng. Perform.* 24 (2014) 694–699.
- [35] H.X. Pei, H.L. Zhang, L.X. Wang, S.L. Li, D.Z. Li, X.T. Wang, Tensile behaviour of 316LN stainless steel at elevated temperatures, *Mater. High Temp.* 31 (2014) 198–203.
- [36] H.Q. Dong, L.M. Yu, Y.C. Liu, C.X. Liu, H.J. Li, J.F. Wu, Effect of hafnium addition on the microstructure and tensile properties of aluminum added high-Cr ODS steels, *J. Alloy. Compd.* 702 (2017) 538–545.
- [37] R.L. Klueh, J.P. Shingledecker, R.W. Swindeman, D.T. Hoelzer, Oxide dispersion-strengthened steels: a comparison of some commercial and experimental alloys, *J. Nucl. Mater.* 341 (2005) 103–114.
- [38] T.J. Zhou, H.S. Ding, X.P. Ma, W. Feng, H.B. Zhao, A.L. Li, Y. Meng, H.X. Zhang, Effect of precipitates on high-temperature tensile strength of a high W-content cast Ni-based superalloy, *J. Alloy. Compd.* 797 (2019) 486–496.
- [39] S. Yokoshima, M. Yamaguchi, Fracture behavior and toughness of PST crystals of TiAl, *Acta Mater.* 44 (1996) 873–883.
- [40] D.R. Johnson, Y. Masuda, H. Inui, M. Yamaguchi, Alignment of the TiAl/Ti₃Al lamellar microstructure in TiAl alloys by growth from a seed material, *Acta Mater.* 45 (1997) 2523–2533.
- [41] J.R. Li, C.L. Zhang, Y.Z. Liu, Influence of carbides on the high-temperature tempered martensite embrittlement of martensitic heat-resistant steels, *Mater. Sci. Eng. A* 670 (2016) 256–263.
- [42] D. Kaoumi, K. Hrutkay, Tensile deformation behavior and microstructure evolution of Ni-based superalloy 617, *J. Nucl. Mater.* 454 (2014) 265–273.
- [43] R. Feng, B. Feng, M.C. Gao, C. Zhang, J.C. Neufeld, J.D. Poplawsky, Y. Ren, K. An, M. Widom, P.K. Liaw, Superior high-temperature strength in a supersaturated refractory high-entropy alloy, *Adv. Mater.* 33 (2021), e2102401.
- [44] W. Jiang, S.Y. Yuan, Y. Cao, Y. Zhang, Y.H. Zhao, Mechanical properties and deformation mechanisms of a Ni₂Co₁Fe₁V_{0.5}Mo_{0.2} medium-entropy alloy at elevated temperatures, *Acta Mater.* 213 (2021), 116982.
- [45] M.E. Kassner, M.T. Pérez-Prado, Five-power-law creep in single phase metals and alloys, *Prog. Mater. Sci.* 45 (2000) 1–102.
- [46] M. Kawasaki, T.G. Langdon, The many facets of deformation mechanism mapping and the application to nanostructured materials, *J. Mater. Res.* 28 (2013) 1827–1834.
- [47] B. Chen, P.E.J. Flewitt, A.C.F. Cocks, D.J. Smith, A review of the changes of internal state related to high temperature creep of polycrystalline metals and alloys, *Int. Mater. Rev.* 60 (2015) 1–29.
- [48] H.T. Jeong, W.J. Kim, Calculation and construction of deformation mechanism maps and processing maps for CoCrFeMnNi and Al_{0.5}CoCrFeMnNi high-entropy alloys, *J. Alloy. Compd.* 869 (2021), 159256.
- [49] W.D. Callister, *Materials Science and Engineering: An Introduction*, 6th ed., John Wiley & Sons, New York, 2007.
- [50] M.T. Perez-Prado, M.E. Kassner, The 3-power-law viscous glide creep. Fundamentals of Creep in Metals and Alloys, 3rd ed., Butterworth-Heinemann, Boston, 2015, pp. 129–138. M.E. Kassner.
- [51] A.C.F. Cocks, M.F. Ashby, On creep fracture by void growth, *Prog. Mater. Sci.* 27 (1982) 189–244.
- [52] H.L. Zhu, O. Muránsky, T. Wei, J. Davis, E. Budzacoska-Testone, H.F. Huang, M. Drew, The effect of applied stress on the high-temperature creep behaviour and microstructure of NiMoCr Hastelloy-N® alloy, *Materialia* 16 (2021), 101069.
- [53] S.D. Antolovich, R.W. Armstrong, Plastic strain localization in metals: origins and consequences, *Prog. Mater. Sci.* 59 (2014) 1–160.
- [54] Y.F. Liu, Y. Cao, Q.Z. Mao, H. Zhou, Y.H. Zhao, W. Jiang, Y. Liu, J.T. Wang, Z. S. You, Y.T. Zhu, Critical microstructures and defects in heterostructured materials and their effects on mechanical properties, *Acta Mater.* 189 (2020) 129–144.
- [55] W. Jiang, H. Zhou, Y. Cao, J.F. Nie, Y.S. Li, Y.H. Zhao, M. Kawasaki, T. G. Langdon, Y.T. Zhu, On the heterogeneity of local shear strain induced by high-pressure torsion, *Adv. Eng. Mater.* 22 (2020), 1900477.
- [56] Y.B. Kang, K.H. Lee, S.I. Hong, Creep behaviors of CrMnFeCoNi high entropy alloy at intermediate temperatures, *Key Eng. Mater.* 737 (2017) 21–26.
- [57] P. Yavari, T.G. Langdon, An examination of the breakdown in creep by viscous glide in solid solution alloys at high stress levels, *Acta Metall.* 30 (1982) 2181–2196.
- [58] V. Šustek, M. Pahutová, J. Čadek, Sigmoidal creep in a Cu-16Al solid solution alloy, *Mater. Sci. Eng. A* 205 (1996) 50–58.
- [59] M. Pahutová, J. Čadek, On two types of creep behaviour of FCC solid solution alloys, *Phys. Status Solidi* 56 (1979) 305–313 (a).
- [60] J.S. Wang, W.D. Nix, High temperature creep and fracture properties of a class I solid solution alloy: Cu-2.7 at.% Sn, *Acta Metall.* 34 (1986) 545–555.
- [61] J.Y. He, H. Wang, Y. Wu, X.J. Liu, T.G. Nieh, Z.P. Lu, High-temperature plastic flow of a precipitation-hardened FeCoNiCr high entropy alloy, *Mater. Sci. Eng. A* 686 (2017) 34–40.
- [62] D. Hull, D.J. Bacon, *Introduction to Dislocations* (Fifth Ed, D. Hull, D.J. Bacon. Jogs and the Intersection of Dislocations, Elsevier, Oxford, 2011, pp. 137–155.
- [63] G.W. Han, I.P. Jones, R.E. Smallman, Direct evidence for Suzuki segregation and Cottrell pinning in MP159 superalloy obtained by FEG(S)TEM/EDX, *Acta Mater.* 51 (2003) 2731–2742.
- [64] G.B. Viswanathan, S. Karthikeyan, R.W. Hayes, M.J. Mills, Creep behaviour of Ti-6Al-2Sn-4Zr-2Mo: II. Mechanisms of deformation, *Acta Mater.* 50 (2002) 4965–4980.
- [65] Y. Cao, S. Ni, X.Z. Liao, M. Song, Y.T. Zhu, Structural evolutions of metallic materials processed by severe plastic deformation, *Mater. Sci. Eng. R* 133 (2018) 1–59.
- [66] H. Siethoff, Cross-slip in the high-temperature deformation of germanium, silicon and indium antimonide, *Philos. Mag. A* 47 (2006) 657–669.
- [67] D. Kuhlmann-Wilsdorf, High-strain dislocation patterning, texture formation and shear banding of wavy glide materials in the LEDS theory, *Scr. Mater.* 36 (1997) 173–181.
- [68] A. Godfrey, Q. Liu, Stored energy and structure in top-down processed nanostructured metals, *Scr. Mater.* 60 (2009) 1050–1055.
- [69] R. Madec, B. Devincere, L. Kubin, T. Hoc, D. Rodney, The role of collinear interaction in dislocation-induced hardening, *Science* 301 (2003) 1879–1882.
- [70] M.S. Soliman, F.A. Mohamed, Creep transitions in an Al-Zn alloy, *Metall. Trans. A* 15 (1984) 1893–1904.
- [71] K.L. Murty, F.A. Mohamed, J.E. Dorn, Viscous glide, dislocation climb and newtonian viscous deformation mechanisms of high temperature creep in Al-3Mg, *Acta Metall.* 20 (1972) 1009–1018.

- [72] J. Li, J. Wu, L. Jin, M. Celikin, F. Wang, S. Dong, J. Dong, The role of dislocation-solute interactions on the creep behaviour of binary Mg-RE alloys, *Sci. Rep.* 11 (2021) 2860.
- [73] W. Blum, P. Eisenlohr, Dislocation mechanics of creep, *Mater. Sci. Eng. A* 510-511 (2009) 7-13.
- [74] F.A. Mohamed, T.G. Langdon, The transition from dislocation climb to viscous glide in creep of solid solution alloys, *Acta Metall.* 22 (1974) 779-788.
- [75] R. Sandström, Basic model for primary and secondary creep in copper, *Acta Mater.* 60 (2012) 314-322.
- [76] H. Laks, C.D. Wiseman, O.D. Sherby, J.E. Dorn, Effect of stress on creep at high temperatures, *J. Appl. Mech.* 24 (1957) 207-213.
- [77] Y.Q. Bu, Y. Wu, Z.F. Lei, X.Y. Yuan, H.H. Wu, X.B. Feng, J.B. Liu, J. Ding, Y. Lu, H. T. Wang, Z.P. Lu, W. Yang, Local chemical fluctuation mediated ductility in body-centered-cubic high-entropy alloys, *Mater. Today* 46 (2021) 28-34.
- [78] J. Moon, S.I. Hong, J.W. Bae, M.J. Jang, D. Yim, H.S. Kim, On the strain rate-dependent deformation mechanism of CoCrFeMnNi high-entropy alloy at liquid nitrogen temperature, *Mater. Res. Lett.* 5 (2017) 472-477.
- [79] S.I. Hong, J. Moon, S.K. Hong, H.S. Kim, Thermally activated deformation and the rate controlling mechanism in CoCrFeMnNi high entropy alloy, *Mater. Sci. Eng. A* 682 (2017) 569-576.
- [80] D.E. Laughlin, K. Hono, N. Hiroshi, *Physical metallurgy. Defects in Metals*, 5th ed., Elsevier, Oxford, 2014, pp. 561-637.
- [81] D. Hull, D.J. Bacon, *Introduction to dislocations*, D. Hull, D.J. Bacon. *Defects in Crystals*, 5th ed., Elsevier, Oxford, 2011, pp. 1-20.
- [82] D. Hull, D.J. Bacon, *Introduction to dislocations*, D. Hull, D.J. Bacon. *Movement of Dislocations*, 5th ed., Elsevier, Oxford, 2011, pp. 43-62.
- [83] S.R. Huang, O. Ozcelik, Q. Gu, A practical and efficient coupling method for large scale soil-structure interaction problems, *Soil Dyn. Earthq. Eng.* 76 (2015) 44-57.
- [84] F. He, Z.J. Wang, Q.F. Wu, D. Chen, T. Yang, J.J. Li, J.C. Wang, C.T. Liu, J.J. Kai, Tuning the defects in face centered cubic high entropy alloy via temperature-dependent stacking fault energy, *Scr. Mater.* 155 (2018) 134-138.
- [85] J.W. Wang, Y. Liu, B. Liu, Y. Wang, Y.K. Cao, T.C. Li, R. Zhou, Flow behavior and microstructures of powder metallurgical CrFeCoNiMo_{0.2} high entropy alloy during high temperature deformation, *Mater. Sci. Eng. A* 689 (2017) 233-242.
- [86] G.J.L. van der Wegen, P.M. Bronsveld, J.T.M. de Hosson, A comparison between different theories predicting the stacking fault energy from extended nodes, *Scr. Metall.* 14 (1980) 285-288.
- [87] Z.J. Zhang, M.M. Mao, J.W. Wang, B. Gludovatz, Z. Zhang, S.X. Mao, E.P. George, Q. Yu, R.O. Ritchie, Nanoscale origins of the damage tolerance of the high-entropy alloy CrMnFeCoNi, *Nat. Commun.* 6 (2015) 10143.
- [88] Y. Zhang, Y.J. Zhou, J.P. Lin, G.L. Chen, P.K. Liaw, Solid-solution phase formation rules for multi-component alloys, *Adv. Eng. Mater.* 10 (2008) 534-538.
- [89] G. Laplanche, P. Gadaud, O. Horst, F. Otto, G. Eggeler, E.P. George, Temperature dependencies of the elastic moduli and thermal expansion coefficient of an equiatomic, single-phase CoCrFeMnNi high-entropy alloy, *J. Alloy. Compd.* 623 (2015) 348-353.
- [90] G. Laplanche, P. Gadaud, C. Bärsch, K. Demtröder, C. Reinhart, J. Schreuer, E. P. George, Elastic moduli and thermal expansion coefficients of medium-entropy subsystems of the CrMnFeCoNi high-entropy alloy, *J. Alloy. Compd.* 746 (2018) 244-255.
- [91] X.P. Du, J.C. Zhao, First measurement of the full elastic constants of Ni-based superalloy René 88DT, *Scr. Mater.* 152 (2018) 24-26.
- [92] T.M. Pollock, S. Tin, Nickel-based superalloys for advanced turbine engines: chemistry, microstructure and properties, *J. Propul. Power* 22 (2006) 361-374.
- [93] H. Takagi, M. Fujiwara, K. Takehi, Measuring Young's modulus of Ni-based superalloy single crystals at elevated temperatures through microindentation, *Mater. Sci. Eng. A* 387-389 (2004) 348-351.
- [94] H.X. Pei, S.L. Li, L.X. Wang, H.L. Zhang, Z.D. Zhao, X.T. Wang, Influence of initial microstructures on deformation behavior of 316LN austenitic steels at 400-900 °C, *J. Mater. Eng. Perform.* 24 (2015) 694-699.
- [95] H. Mirzadeh, J.M. Cabrera, A. Najafzadeh, Constitutive relationships for hot deformation of austenite, *Acta Mater.* 59 (2011) 6441-6448.
- [96] Y. Wang, W.Z. Shao, L. Zhen, C. Yang, X.M. Zhang, Tensile deformation behavior of superalloy 718 at elevated temperatures, *J. Alloy. Compd.* 471 (2009) 331-335.
- [97] S. Majumdar, S. Raveendra, I. Samajdar, P. Bhargava, I.G. Sharma, Densification and grain growth during isothermal sintering of Mo and mechanically alloyed Mo-TZM, *Acta Mater.* 57 (2009) 4158-4168.
- [98] B. Paul, D. Jain, S.P. Chakraborty, I.G. Sharma, C.G.S. Pillai, A.K. Suri, Sintering kinetics study of mechanically alloyed nanocrystalline Mo-30wt.% W, *Thermochim. Acta* 512 (2011) 134-141.
- [99] J. Ciulik, E.M. Taleff, Power-law creep of powder-metallurgy grade molybdenum sheet, *Mater. Sci. Eng. A* 463 (2007) 197-202.
- [100] A.N. Campbell, S.S. Tsao, D. Turnbull, The effect of Au and Ag additions on the power-law creep behavior of Pb, *Acta Metall.* 35 (1987) 2453-2464.
- [101] J.Y. He, C. Zhu, D.Q. Zhou, W.H. Liu, T.G. Nieh, Z.P. Lu, Steady state flow of the FeCoNiCrMn high entropy alloy at elevated temperatures, *Intermetallics* 55 (2014) 9-14.